

RESEARCH ARTICLE | JANUARY 29 2025

FreeMHD: Validation and verification of the open-source, multi-domain, multi-phase solver for electrically conductive flows

Brian Wynne ; Francisco Saenz ; Jabir Al-Salami ; Yufan Xu ; Zhen Sun ; Changhong Hu ; Kazuaki Hanada ; Egemen Kolemen  



Phys. Plasmas 32, 013907 (2025)

<https://doi.org/10.1063/5.0230242>

 CHORUS



Articles You May Be Interested In

KoopmanLab: Machine learning for solving complex physics equations

APL Mach. Learn. (September 2023)

Experimental realization of a quantum classification: Bell state measurement via machine learning

APL Mach. Learn. (September 2023)



Physics of Plasmas

Special Topics Open
for Submissions

[Learn More](#)

FreeMHD: Validation and verification of the open-source, multi-domain, multi-phase solver for electrically conductive flows

Cite as: Phys. Plasmas **32**, 013907 (2025); doi: [10.1063/5.0230242](https://doi.org/10.1063/5.0230242)

Submitted: 22 July 2024 · Accepted: 2 January 2025 ·

Published Online: 29 January 2025



View Online



Export Citation



CrossMark

Brian Wynne,¹ Francisco Saenz,¹ Jabir Al-Salami,² Yufan Xu,³ Zhen Sun,³ Changhong Hu,² Kazuaki Hanada,² and Egemen Kolemen^{1,3,a)}

AFFILIATIONS

¹Department of Mechanical and Aerospace Engineering, Princeton University, Princeton, New Jersey 08540, USA

²Research Institute for Applied Mechanics, Kyushu University, Kasuga, Fukuoka 816-8580, Japan

³Princeton Plasma Physics Laboratory, Princeton, New Jersey 08540, USA

^{a)} Author to whom correspondence should be addressed: ekolemen@pppl.gov

ABSTRACT

The extreme heat fluxes in the divertor region of tokamaks may require an alternative to solid plasma-facing components, for the extraction of heat and the protection of the surrounding walls. Flowing liquid metals are proposed as an alternative, but raise additional challenges that require investigation and numerical simulations. Free surface designs are desirable for plasma-facing components, but steady flow profiles and surface stability must be ensured to limit undesirable interactions with the plasma. Previous studies have mainly used steady-state, 2D, or simplified models for internal flows and have not been able to adequately model free-surface liquid metal (LM) experiments. Therefore, FreeMHD has been recently developed as an open-source magnetohydrodynamics (MHD) solver for free-surface electrically conductive flows subject to a strong external magnetic field. The FreeMHD solver computes incompressible free-surface flows with multi-region coupling for the investigation of MHD phenomena involving fluid and solid domains. The model utilizes the finite-volume OpenFOAM framework under the low magnetic Reynolds number approximation. FreeMHD is validated using analytical solutions for the velocity profiles of closed channel flows with various Hartmann numbers and wall conductance ratios. Next, experimental measurements are then used to verify FreeMHD, through a series of cases involving dam breaking, 3D magnetic fields, and free-surface LM flows. These results demonstrate that FreeMHD is a reliable tool for the design of LM systems under free surface conditions at the reactor scale. Furthermore, it is flexible, computationally inexpensive, and can be used to solve fully 3D transient MHD flows.

© 2025 Author(s). All article content, except where otherwise noted, is licensed under a Creative Commons Attribution (CC BY) license (<https://creativecommons.org/licenses/by/4.0/>). <https://doi.org/10.1063/5.0230242>

NOMENCLATURE

B	Magnetic field (T)
<i>B</i>	Magnetic field magnitude (T)
<i>D</i>	Volume domain (m ³)
F_g	Gravity volume force (N/m ³)
F_L	Lorentz volume force (N/m ³)
F_{ST}	Surface tension volume force (N/m ³)
g	Gravity vector (m ² /s)
J	Electric current density (A/m ²)
<i>h</i>	Fluid height (m)
<i>L</i>	Channel length (m)
<i>ℓ</i>	Channel half-width (m)

<i>N_f</i>	Number of faces
n	Normal vector
<i>p</i>	Fluid pressure (Pa)
<i>p'</i>	Alternative fluid pressure (Pa)
S_f	Surface normal vector
U	Fluid velocity (m/s)
<i>U</i>	Fluid velocity magnitude (m/s)
<i>V_C</i>	Cell volume (m ³)
x	Position vector (m)
<i>α</i>	Volume fraction
<i>Δt</i>	Time step (s)
<i>Δx</i>	Cell length (m)
<i>γ_{st}</i>	Fluid surface tension coefficient (N/m)

κ	Curvature vector (1/m)
μ_0	Vacuum permeability (N/A ²)
ρ	Fluid density (kg/m ³)
σ	Fluid electrical conductivity (S/m)
σ_w	Solid wall electrical conductivity (S/m)
τ	Viscous stress tensor (Pa)

I. INTRODUCTION

A remaining challenge in the pursuit of fusion energy is handling large heat and particle fluxes. These can be especially damaging to the interior of the reactor, specifically in the divertor region.¹ An alternative is to use a liquid metal (LM) to provide a self-healing and replenishing surface. A LM with a free surface could serve as the plasma-facing component, offering advantages such as heat transfer through convection and eliminating erosion and the need for component replacement. Additionally, some LM designs can offer low hydrogen recycling regimes, meaning that the excess fuel encountering the surface stays in the LM instead of returning to the plasma.² Lithium, for example, has been shown to reduce tritium recycling, with a key benefit being an increase in plasma performance.^{3,4}

However, along with the advantages come additional challenges that must be solved. One such challenge is reducing the opposing Lorentz force, which acts as a magnetohydrodynamic (MHD) drag to cause a pileup of flow across a magnetic field.⁵ Other challenges involve flow separation, droplet ejection, and keeping the surface as flat as possible to avoid surface deformities, which would collect a large heat flux from the exhaust plasma at a shallow angle in the divertor, leading to concerns of evaporation or splashing.⁶

In order to address these challenges, a key step is the development of numerical solvers that can simulate the behavior of conductive flows across magnetic fields. The primary motivation is to develop reliable computational code that can accurately predict and replicate real flows under laboratory conditions, thereby enabling simulations under reactor regimes and informing the design of future fusion experiments. Existing challenges include the computational complexity and memory-intensive nature of simulating multi-phase, three-dimensional flows, and electric currents with free surfaces.

Previous studies have mainly used steady-state, 2D, or simplified models for internal flows and have not been able to adequately model free-surface LM experiments. A 2D model was developed for studying a magnetic field gradient for film flow.⁷ This model predicted the negative effects of flows across these fields such as hydraulic jump-like patterns forming, but did not include all the effects involving recirculating currents. Subsequently, a 3D code was developed for free surface flows using induced-magnetic field equations and confirmed the need for 3D codes to capture phenomena that could not be described by 2D simulations.⁸ Simulations using HyPerComp Incompressible MHD solver for Arbitrary Geometries (HIMAG) were developed for predicting and modeling the effects of the magnetic environment on the flow characteristics of the LM flows using the electric potential formulation.⁹ However, HIMAG is not open-source or as flexible as OpenFOAM-based solvers. In the last few years, additional studies have looked at both open source and commercial solvers. In one instance, numerical simulations have been performed for an open-surface lithium divertor using reduced-order flow models involving multiphase MHD flow in OpenFOAM.¹⁰ Another example is a customized version of the general-purpose CFD in ANSYS CFX for

complex 3D geometries using the magnetic vector potential MHD formulation.¹¹

Recently, a set of incompressible MHD flow solvers have been developed, with one solver for single-phase flow in multiple electro-coupled domains and one solver for two-phase flows.¹² However, these solvers are currently separate and not yet integrated, and therefore are not equipped to solve free-surface bulk flow with strong magnetic fields. Therefore, an open-source computational model capable of accurately simulating 3D free-surface liquid metal flows in the presence of applied magnetic fields is needed, as previous examples lack flexibility, open-source availability, and the ability to adequately model relevant plasma-facing component experiments.

In response to this need, MHD OpenFOAM solvers have been developed¹³ and have now been formalized and called FreeMHD¹⁴ as open-source, custom simulations to compute multi-region, free-surface flows in magnetic fields. FreeMHD is a useful tool for the fusion community, offering the ability to solve design and implementation problems for LM PFC research. Moreover, it is open-source, readily available for use, and fully parallelized for CPUs. FreeMHD is a comprehensive solver for free surface liquid MHD flows and can be used for any flow with MHD conditions.

The verification of FreeMHD is presented using cases of closed flow in ducts through comparison to analytical solutions. The validation of FreeMHD involves comparison to experiments to determine the accuracy of the model in simulating various phenomena. The first case of a pipe with 3D magnetic profiles, tests the ability of FreeMHD to calculate this current distribution in strong spatially varying magnetic fields. Next, the dam breaking case was chosen to test the evolution of the free surface flows. Finally, the LMX-U and Divertorlets cases combine these effects by testing free-surface flows with magnetic fields. While one of the main applications is with liquid lithium for fusion applications, the validation cases presented use galinstan and sodium-potassium alloys to compare with experimental results.

The objective of this study is to describe FreeMHD, present the validation and verification, and explain the utility of the computational solver for magnetohydrodynamics and fusion-related applications. This paper seeks to describe the motivation and need for these new developments, provide details on the model, and explain how it is implemented. It is the contention of this paper that the open-source nature of FreeMHD enables future development, allowing further improvements and additional features to be added. Throughout, it will be shown that the validation of FreeMHD with experiments has been successful and that FreeMHD provides a fast, accurate, and accessible way to model free-surface liquid metal flows under fusion-relevant conditions. This enables the planning and testing of divertor concepts in tokamak reactors.

Section II discusses the mathematical model, while Sec. III describes the numerical method, solver specifications, and the cases tested. Section IV presents the results of the validation and verification, and Sec. V provides a discussion of the results and applications. Finally, Sec. VI summarizes and suggests future directions and development.

II. MATHEMATICAL MODELS

A. Governing equations

The modeling of electrically conductive flow begins with using the incompressible, Eulerian form of the Navier–Stokes equations

$$\frac{\partial \rho}{\partial t} + \nabla \cdot (\rho \mathbf{U}) = 0, \quad (1)$$

$$\frac{\partial \rho \mathbf{U}}{\partial t} + \nabla \cdot (\rho \mathbf{U} \otimes \mathbf{U}) = -\nabla p + \nabla \cdot \underline{\underline{\tau}} + \mathbf{F}_g + \mathbf{F}_{ST} + \mathbf{F}_L, \quad (2)$$

for the conservation of mass and momentum, with parameters defined in the Nomenclature. An alternative pressure was defined for numerical convenience, $p' = p - \rho(\mathbf{g} \cdot \mathbf{x})$. The viscous stress tensor is represented by $\underline{\underline{\tau}} = \mu(\nabla \mathbf{U} + (\nabla \mathbf{U})^T)$.

The finite volume OpenFOAM framework with the volume of fluid (VoF) method is used for interface capturing, where a function $I(\mathbf{x}, t)$ is defined at each point and is equal to 1 or 0 to indicate fluids 1 or 2, over the volume domain D . Then, the volume fraction in a control volume D_i within D is defined as

$$\alpha_i = \frac{1}{|D_i|} \int_{D_i} I(\mathbf{x}, t) dV \quad (3)$$

over the domain. The evolution of the volume fraction for an incompressible flow is described by

$$\frac{\partial \alpha}{\partial t} + \nabla \cdot (\alpha \mathbf{U}) = 0. \quad (4)$$

The physical properties of the fluid in each cell are calculated from the volume fraction using

$$\xi = \alpha \xi_1 + (1 - \alpha) \xi_2, \quad (5)$$

where ξ_1 and ξ_2 correspond to the fluid properties of fluids 1 and 2, and ξ represents ρ , μ , and σ for density, viscosity, and electrical conductivity, respectively. Finally, the surface tension force between the gas-liquid interface is modeled using the continuum surface force (CSF) method.¹⁵ Here, the force due to surface tension is calculated as $\mathbf{F}_{st} = \gamma_{st} \kappa \nabla \alpha$, and has been included as a body force in the momentum balance. Here, $\kappa = \nabla \cdot (\nabla \alpha / |\nabla \alpha|)$ is the curvature vector between the fluid-fluid interface and γ_{st} is the fluid surface tension coefficient.

The magnetic Reynolds number is defined as $Re_m = \mu_0 \sigma U \ell$, for characteristic values of velocity U , length ℓ , and fluid conductivity σ , where μ_0 is the vacuum permeability.

Re_m represents the ratio of convection to diffusion of the magnetic field, and for $Re_m \ll 1$, diffusion is dominated and the induced magnetic field due to induced currents can generally be neglected when compared to the applied magnetic field B .¹⁶ The result is that the magnetic field is essentially unaffected by the flow, and instead of a magnetic field being coupled with the velocity field, one can just consider the velocity field coupled to the background magnetic field.

This is known as the inductionless approximation and allows the electric field to be expressed as the gradient of the scalar electric potential ($\mathbf{E} = -\nabla \phi$).¹⁷ Then from Ohm's law

$$\mathbf{J} = \sigma(-\nabla \phi + (\mathbf{U} \times \mathbf{B})) \quad (6)$$

and conservation of current density

$$\nabla \cdot \mathbf{J} = 0, \quad (7)$$

the electric potential Poisson equation is expressed as

$$\nabla \cdot (\sigma \nabla \phi) = \nabla \cdot ((\sigma \mathbf{U}) \times \mathbf{B}). \quad (8)$$

This is discretized for each face f ,

$$\sum_{f=1}^{N_f} \left[\sigma \frac{\partial \phi}{\partial \mathbf{n}} \right]_f = \sum_{f=1}^{N_f} [\sigma (\mathbf{U} \times \mathbf{B}) \cdot \mathbf{S}]_f \quad (9)$$

for N_f number of faces, and is then used to solve for the electric potential ϕ .

The electric current density at the cell faces is calculated using variables evaluated at each face center

$$J_{nf} = \left[\sigma \left(-\frac{\partial \phi}{\partial \mathbf{n}} S + (\mathbf{U} \times \mathbf{B}) \cdot \mathbf{n} \right) \right]_f. \quad (10)$$

Then the Lorentz force (F_L) is calculated using its conservative form and reconstructed to the cell center for each cell C with

$$(J \times B)_C = -\frac{1}{V_C} \sum_{f=1}^{N_f} J_{nf} (\mathbf{B} \times \mathbf{xS})_f - \mathbf{x}_C \times \left[\frac{1}{V_C} \sum_{f=1}^{N_f} J_{nf} (\mathbf{BS})_f \right] \quad (11)$$

following a conservative scheme for calculating the Lorentz force.¹⁸

Additionally, an energy equation for heat transfer is included in FreeMHD as an option, but is not needed for these cases as the liquid metals are considered to be at constant temperatures and incompressible.

B. Boundary conditions

The boundary conditions involve flow variables of velocity and pressure, as well as electric potential and must be defined for all boundaries such as inlets, outlets, openings to the atmosphere, and interfaces between fluid and solid regions. The flow variable boundary condition at the inlet can be generally set through a fixed velocity, fixed pressure, or a fully developed velocity profile. For a set velocity, the pressure at the inlet is then set to a zero gradient. For the outlet, a Dirichlet boundary condition is typically used for pressure at a reference value. For the top opening, the total pressure is fixed, allowing gas flow in or out. At the interface of fluid and solid walls, the gas and liquid boundary conditions involve the no-slip velocity condition ($\mathbf{U} = 0$). Additionally, considering the volume fraction for the free surface, a fixed contact angle is set for surface tension effects at the wall. The pressure at the wall is defined by a Neumann boundary condition, with the pressure gradient $\partial p' / \partial \mathbf{n}$, such that the flux on the boundary is specified by the velocity condition, here the no-slip walls, where \mathbf{n} is the wall normal vector. Electric current conservation at the inlet and outlet can be imposed by ensuring no electric current enters or exits through these boundaries, by setting $\partial \phi / \partial \mathbf{n} = (\mathbf{U} \times \mathbf{B}) \cdot \mathbf{n}$. When applying an external current density, the electric potential gradient at the boundary was set based on $\nabla \phi = \pm I_0 / (A \sigma_w)$, where I_0 is the applied current in Amperes, A is the area of the boundary in meters, and σ_w is the electric conductivity of the solid wall in siemens per meter.

III. NUMERICAL METHODS

A. Solver specifications

The primary electric potential solver of FreeMHD is called `epotMultiRegionInterFoam`, which is discretized with implicit

Euler time-stepping. Despite its first-order accuracy, this scheme's stability allows for taking large time steps, which helps carry out efficient simulations of transient phenomena.

FreeMHD has been tested and used in parallel and is typically run with CPUs on Princeton's Stellar and Della clusters. Table I contains examples of the CPU Hours and time to run on the cluster for the Shercliff, Dam Breaking, and LMX-U cases. Additionally, the typical cell size and maximum time step are listed for reference.

The pressure-velocity coupling method uses the pressure implicit with splitting of operations (PISO) algorithm, for coupling the continuity and momentum equations.¹⁹ For both solid and fluid regions, the electrical potential equation is solved. Additionally, for fluid regions, there is an interface-capturing procedure, then the density is updated, the velocity flux is calculated for each phase, and then the current density is calculated. For both solid and fluid regions, the boundary conditions can be updated and looped again or advance to the next time step. The PISO loop is completed to obtain the corrected velocity and is combined with additional iterations that include the solid regions, so the solution process becomes similar to a combination of the PISO and SIMPLE (semi-implicit method for pressure-linked equations)^{20,21} algorithms. The fluid and solid regions are coupled by solving each one separately and then exchanging information through boundary conditions that contain details from the neighboring region. This requires outer loops to ensure proper coupling within each time step. Additional details on the algorithm can be found in Appendix A.

For interface capturing, the MULTidimensional Limiter for Explicit Solution (MULES) method modifies the advection of the volume fraction by adding an interface compression velocity term. This method controls the thickness and reduces smearing of the interface.¹³

The fluid flow behavior can be characterized by a variety of non-dimensional parameters. The Reynolds number ($Re = U\ell/\nu$) represents the ratio of inertial to viscous forces, where U , ℓ , and ν are, respectively, characteristic values of velocity, length, and kinematic viscosity on a per-case basis. The interaction parameter ($N = (\sigma\ell B^2)/(\rho U)$) is the ratio of electromagnetic to inertial forces, where σ , B , and ρ are characteristic values of the fluid electrical conductivity, externally applied magnetic field, and fluid density, respectively. The Reynolds number and interaction parameter are derived from the non-dimensionalization of the momentum equation.¹⁷

In applications with magnetic fields, an important balance of forces is between the electromagnetic and viscous forces, which is based on the combination of the Reynolds number and the interaction parameter $ReN = Ha^2$, where the inertial forces cancel to leave the ratio of electromagnetic and viscous forces in terms of the squared Hartmann number.¹⁶ Here, Ha^2 is the ratio of magnetic

and viscous forces where the Hartmann number ($Ha = B\ell\sqrt{\sigma/(\rho\nu)}$) itself is commonly used to express the relative strength of the magnetic field.

For flows involving a magnetic field, the turbulence can be considered suppressed based on the ratio of the Reynolds number and Hartmann number. This suppression of turbulence is characterized by the critical value of the ratio of the Reynolds and Hartmann numbers ($R = Re/Ha$), which was experimentally found to be approximately $R_{crit} = 380$ through a transition to turbulence in the Hartmann layer electromagnetic flow in a square duct.²² This ratio can be interpreted as the Reynolds number based on the thickness of the Hartmann layer and indicates that the magnetic field can suppress turbulence for cases of R lower than the critical value.

For cases with no magnetic fields (Dam Breaking and LMX with no magnetic field), the value of $R > R_{crit}$. Therefore, here a turbulence model is used, since in this regime, turbulence cannot be assumed to be suppressed and needs to be modeled. The standard $k-\epsilon$ model was chosen due to its reliability and relative ease of use, and common usage in CFD simulations, where it has been used successfully in open channel flows.^{23,24} This involved only slight changes to the case setup, involving the initial and boundary conditions of the turbulence variables, as well as the inclusion of the $k-\epsilon$ turbulence equations. Conversely, for all cases with magnetic fields, the setup does not include any turbulence equations, and therefore no MHD turbulence is considered.

B. Conditions for numerical stability and accuracy

The Courant number describes how fast a fluid travels across a grid of cell length Δx in time Δt , with a characteristic velocity U , and is generally defined as $Co = U\Delta t/\Delta x$. Extending to a discretized form, the volumetric flux is first evaluated using the scalar product of velocity U_f and the surface normal vector S_f of face f , and then summed for all N_f faces. Then the time step Δt and cell volume V_C of a cell C are used to calculate $Co_C = \frac{\Delta t}{2V_C} \sum_{f=1}^{N_f} U_f \cdot S_f$ for all cells. The Courant-Friedrichs-Lewy (CFL) condition states that $Co \leq Co_{C,max}$, where $Co_{C,max}$ is typically less than or equal to one. With a stationary grid, this is implemented by limiting the time step such that the maximum courant number is not exceeded.

The Alfvén velocity ($v_A = B/\sqrt{\mu_0\rho}$) is the speed at which Alfvén waves propagate and indicates how quickly disturbances in the magnetic field are communicated through the fluid. This can be useful in predicting and controlling the stability of liquid metal flows, and characteristic values for galinstan, NaK, and lithium are listed in Table II along with the corresponding Alfvén time ($\tau_A = \ell/v_A$) based on a length scale (ℓ). Next, the magnetic damping time is calculated from values of the fluid density, electrical conductivity, and a characteristic

TABLE I. Parallelization and solver times for the Shercliff, Dam Breaking, and LMX-U cases.

Case	CPU hours	Time to run (h)	Cell size (μm)	Time step (ms)
Closed channel	12	1	1–1000	0.01–1
Free surface, Dam breaking	47.3	1.3	500	1
Free surface, LMX-U	1865	12	500	0.2

TABLE II. Alfvén velocity, Alfvén time, and magnetic damping time for galinstan, NaK, and lithium.

Material	Alfvén velocity, v_A (m/s)	Alfvén time, τ_A (s)	Magnetic damping time, τ_B (s)
Galinstan	151.35	3.30×10^{-4}	2.28×10^{-2}
NaK	370.57	1.46×10^{-4}	3.22×10^{-4}
Lithium	3970.02	2.52×10^{-5}	5.89×10^{-6}

magnetic field, $\tau_B = \rho/(\sigma B^2)$, and represents the timescale on how quickly the magnetic field can dissipate the kinetic energy of the flow. The solver time step Δt should be less than τ_B , with typical values in Table II.

C. Cases tested

For verification and validation, a variety of setups under various conditions are presented. For these cases, the properties of liquid metals galinstan, NaK, and lithium are shown in Table III. Here, galinstan and NaK are used in experimental validation cases, while lithium is included for comparison as a prominent option for application into reactors as a plasma-facing component. Galinstan is significantly more dense than NaK and lithium, but has a similar electrical conductivity, meaning similar effects can be observed in flows across magnetic fields. Dimensionless parameters can be used to scale results for comparison of liquid metals with different properties.

For these studies, non-dimensional parameters are useful for the characterization of the regime of the various flows, using the fluid properties as well as characteristic scales for the flow and geometrical parameters. For instance, the characteristic length for the Hartmann number is typically half of the distance across the direction parallel to the magnetic field. In closed channels, this length could be the half-width of a rectangular duct or the radius of a circular pipe. The magnetic bond number (Bo_m) is the ratio of magnetic Lorentz forces to surface tension forces, which is typically expressed as $(B^2 \ell)/(\mu_0 \sigma_{st})$ but here will be taken as $Bo_m = (JB)/(\sigma_{st}/\ell^2)$, to consider the applied or induced current density (J). Finally, the wall conductance ratio is $c = (\sigma_w t_w)/(\sigma \ell)$, where σ_w and t_w are the electrical conductivity and thickness of the solid wall. The wall conductance ratio affects the distribution of electric currents in the fluid and the surrounding solid, and consequently alters the MHD effects on the flow.

For numerical verification, two classic cases involving liquid metal flows in square ducts across transverse magnetic fields will be compared to analytical solutions. First, the Shercliff case is a closed channel duct with all insulating walls.²⁸ Second, the Hunt case (case II) is also a closed channel duct, but by contrast to the Shercliff case has conducting walls perpendicular to the magnetic field and insulating walls parallel to the magnetic field.²⁹ Figure 1(a) shows the setup for

the Shercliff and Hunt cases, which are treated here as having a wall conductance ratio of $c = 0$ and 0.05, respectively. In both cases, the presence of the magnetic field alters the boundary layer structure, reducing the boundary layer thickness—i.e., the distance to where the flow reaches its bulk flow velocity. The Hartmann layer thickness scales as $1/Ha$, so this boundary layer becomes very thin with increasing magnetic field magnitude, requiring higher density mesh close to the wall to be resolved. To ensure the changes in velocity and electric potential are captured, at least 10 cells are included in the boundary layer.

The initial conditions involve a set fluid velocity, with the same velocity as the inlet condition. The outlet is set with a Dirichlet boundary condition of a fixed pressure at a reference value. The transverse magnetic field is ramped up from zero to a fixed uniform value, and the flow is allowed to develop. The 3D channel must be long enough to approach the fully developed solution. The magnetic field is the parameter scanned to obtain the desired Hartmann number, shown here up to $Ha = 1000$.

Next, a variety of cases were chosen for experimental validation. These cases test the ability of FreeMHD in various conditions such as fringing magnetic fields, free surface evolution with no magnetic fields, and then combined with magnetic fields and free surface flows.

The first case for experimental validation, the fringing magnetic field, involves sodium potassium (NaK) flow through a dipole magnet in a closed pipe with electrically conducting walls.³⁰ The experimental measurements focus on the region entering the magnet as shown in Fig. 1(b).

Similar to the Shercliff and Hunt cases, the initial and inlet condition is a set fluid velocity, with the outlet at a fixed pressure. The transverse magnetic field is ramped up from zero, but this time varies along the streamwise direction. A pipe radius of 0.0486 m, maximum magnetic field of 0.682 T, and average velocity of 0.362 m/s are used as characteristic values for the non-dimensionalization. These parameters with the NaK properties from Table III are used for a Reynolds number of 20 000 and Hartmann number of 2000, for experimental comparison.

The next experimental validation case involves a dam breaking case setup, with water in a channel initially at rest and then released, with the free surface profile being measured.³¹ The case setup is shown

TABLE III. Properties of liquid metals: Galinstan (eutectic gallium–indium–tin alloy, 67% Ga, 20.5% In, 12.5% Sn at 20 °C),²⁵ NaK (eutectic sodium–potassium alloy, 22% Na 78% K at 20 °C),²⁶ and lithium (at 250 °C).²⁷

Material	Density, ρ (kg/m ³)	Kinematic viscosity, ν (m ² /s)	Electrical conductivity, σ (S/m)	Surface tension, σ_{st} (N/m)
Galinstan	6360	2.98×10^{-7}	3.10×10^6	0.533
NaK	868.2	1.05×10^{-6}	2.879×10^6	...
Lithium	510	1.13×10^{-6}	3.64×10^6	...

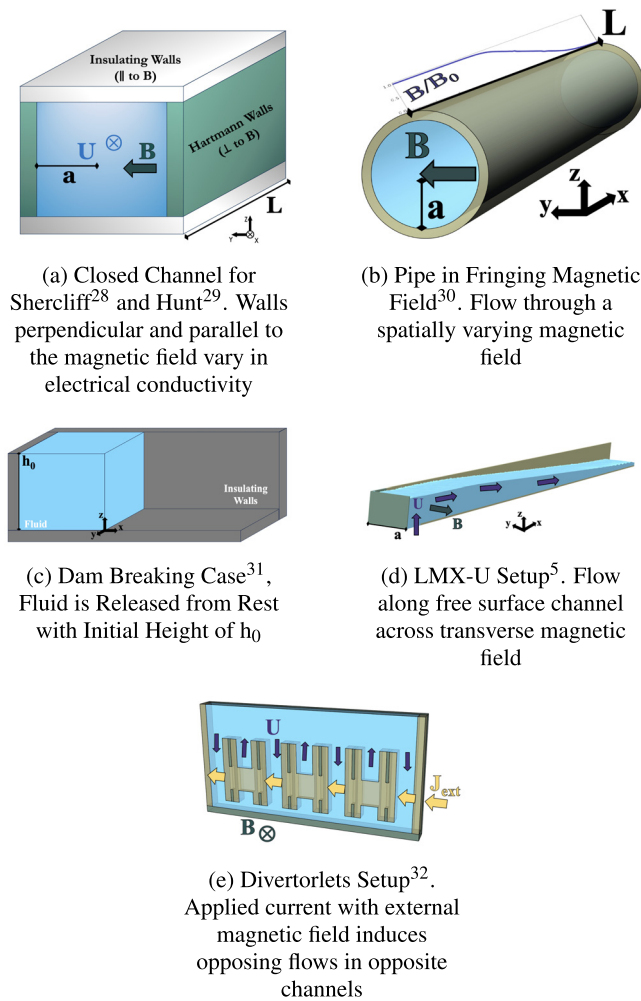


FIG. 1. Diagram and setup for each case: (a) closed channel for Shercliff²⁸ and Hunt.²⁹ Walls perpendicular and parallel to the magnetic field vary in electrical conductivity; (b) pipe in fringing magnetic field.³⁰ Flow through a spatially varying magnetic field; (c) Dam Breaking case.³¹ Fluid is released from rest with initial height of h_0 ; (d) LMX-U setup.⁵ Flow along free surface channel across transverse magnetic field; (e) Divertorlets setup.³² Applied current with external magnetic field induces opposing flows in opposite channels.

in Fig. 1(c), where the initial height is h_0 which is used for scaling the results. The characteristic velocity can be taken as $\sqrt{gh_0}$, with a characteristic length of h_0 to give a Reynolds number of 3.9×10^5 . The initial conditions involve no flow, but the volume fraction is set such that the liquid is in the position of a dam set to release. No inlet or outlet is required as the liquid remains in the domain and only flows down the channel. This case has no magnetic field but is applicable because it provides a validation of the time evolution of the free surface. This ensures that the volume of fluid method is able to capture the time-dependent effects of two-fluid systems. Additionally, this validation confirms the volume fraction is being advected accurately through the VoF schemes.

Another case for comparison is the Liquid Metal eXperiment Upgrade (LMX-U), which is a test bed for liquid metal experiments

with a flow loop and free surface channel.⁵ The LMX-U results are used for free-surface liquid metal flow experimental validation using galinstan, where Fig. 1(d) shows the setup. In this case, the inlet is vertical, and the flow levels off downstream, with a channel length of $L = 1.2$ m from inlet to outlet. Another characteristic length for an open channel is the hydraulic radius ($r_H = A/P$), the ratio of the cross-sectional area of the fluid ($A = hw$) divided by the wetted perimeter ($P = 2h + w$). For LMX-U, with an average height (h) of 2 cm and width (w) of 10 cm, the hydraulic radius is 1.4 cm. With flow rate (Q) in the experiment at 16.3 L/min, the average velocity is $Q/A = 0.1358$ m/s. Therefore, using the hydraulic radius and average velocity as the characteristic length and velocity, the Reynolds number is 6380. The main characteristic length is the channel half-width, $\ell = 0.05$ m, which is used for the non-dimensionalization of the results on the x axis for the flow direction and the fluid height. This length is also used when calculating the Hartmann number. The free surface of galinstan flows across the transverse magnetic field, which varies in the streamwise direction, where the magnet is located from $x/\ell = 0-14.8$. The inlet is from below vertically, with a fixed flow rate, and the outlet has a fixed pressure condition. The test cases of magnetic field strengths of 0.3, 0.2, and 0 T therefore correspond to Hartmann numbers of 607, 404, and 0. For the $Ha = 0$ case, a turbulence model was used ($k-\epsilon$), as the turbulence was not suppressed. The wall conductance ratio with a copper liner is approximately 0.8. For the magnetic bond number, taking σUB as a representative scale for J from Ohm's law [Eq. (6)], the 0.2 and 0.3 T cases correspond to $Bo_m = (\sigma UB^2)/(\sigma_{st}/\ell^2) = 79$ and 180.

Divertorlets is the last case for experimental validation, and represents an alternative LM-PFC design, with applied currents inducing flows between slats.³² As with LMX-U, this device has been tested at PPPL using galinstan, and the Divertorlets results are used for further free-surface liquid metal flow experimental validation, with Fig. 1(e) showing the setup. A current density (J_{ext}) is applied across an array of conductors, such that in opposite channels the electric current is primarily contained in the conductor or in the liquid metal. The external magnetic field, such as the toroidal field in the divertor region of a tokamak, then creates the Lorentz ($J \times B$) force. Due to the varying current density, the opposing channels have strong and weaker downward Lorentz forces, leading to flow recirculating around the conductors. In order to compare to experimental results, simulations are run using applied currents of 400–900 A, corresponding to current densities of approximately $1.9 \times 10^5 - 4.3 \times 10^5$ A/m². A characteristic length and velocity can be taken as the distance between channel slats (5.1 mm) and the average vertical velocity between channels (0.25 m/s), to give a Reynolds number of 4279. The half-width between channel slats (2.55 mm) and the applied magnetic field (0.2 T) is used for a Hartmann number of 21. For the magnetic bond number, using the current densities applied over the applied currents of 400–900 A gives Bo_m from 1.85 to 4.20. With an average magnetic bond number of 3.0 over the parameter scan, this indicates a close balance between the magnetic and surface tension forces.

The applicable non-dimensional parameters for each case are summarized in Table IV: the Reynolds number, Hartmann number, interaction parameter, magnetic Reynolds number, and magnetic bond number.

Furthermore, the ratio of the Reynolds and Hartmann numbers ($R = Re/Ha$) for the Closed Channel Duct, Pipe Fringing B Field, LMX-U with B Field, and Divertorlets are 1.0×10^{-1} , 1.0×10^1 ,

TABLE IV. Characteristic non-dimensional parameters.

Case name	Re	Ha	N	Re _m	Bo _m
Closed channel duct	1.0×10^2	1.0×10^3	1.0×10^4	1.2×10^{-1}	–
Pipe fringing B field	2.0×10^4	2.0×10^3	2.0×10^2	6.4×10^{-2}	–
Dam breaking	3.9×10^5	–	–	–	–
LMX-U	6.4×10^3	6.1×10^2	5.8×10^1	2.6×10^{-2}	1.8×10^2
Divertorlets	4.3×10^3	2.1×10^1	1×10^{-1}	5.0×10^{-3}	3.0×10^0

1.0×10^1 , and 2.0×10^2 , which are all less than the critical value of approximately $R_{crit} = 380$, indicating that turbulence is suppressed. As mentioned in Sec. III, for cases with no magnetic fields (Dam Breaking and LMX-U with no magnetic field), the value of R_{crit} is exceeded, and the standard $k-\epsilon$ model is used.

D. Mesh generation

The built-in OpenFOAM `blockMesh` was used for rectangular channels with various regions for the closed channel cases. Cylindrical mesh generation required special consideration, with a `M4` script to specify meshes for the fringing magnetic field in a pipe case. Another option used is `snappyHexMesh`, which is useful for boundary layers on geometries that do not form straightforward boxes or cylinders, such as the Divertorlets case. A final meshing generation option has been done with Salome, an open-source software, which is converted to OpenFOAM meshes using the `ideasUnvToFoam` conversion. Examples of the meshes for the cases tested are shown in Fig. 2.

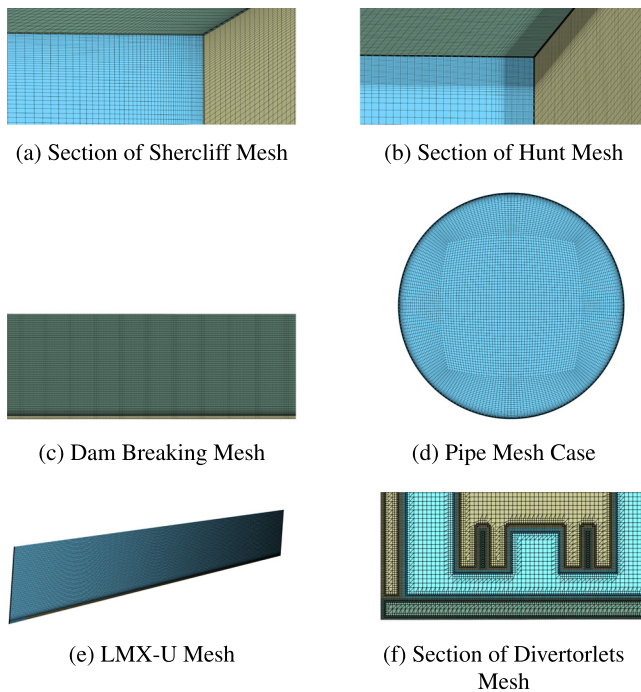


FIG. 2. Examples of meshes used for each case: (a) section of Shercliff mesh, (b) section of Hunt mesh, (c) Dam Breaking mesh, (d) pipe mesh case, (e) LMX-U mesh, and (f) section of Divertorlets mesh.

IV. RESULTS

A. Verification with analytical solutions: Shercliff and Hunt flow

To verify the model, FreeMHD can be compared to theoretical results for which there are analytical solutions. Here, a reformulation of Hunt's equation for velocity profiles of fully developed MHD flows for high Hartmann numbers will be utilized.¹⁸ The reformulation of the analytical solutions is provided in Appendix B. FreeMHD is verified using these analytical solutions for closed channel flows by examining the effect on the closed channel velocity profile and pressure drop while varying the Hartmann number and wall conductance ratio. The two cases presented here are validated using 3D geometry, with channels long enough for the flow to become fully developed.

The validation results for the Shercliff case are shown in Figs. 3(a) and 3(b) for the Hartmann layer and side layer, plotting the normalized velocity profile across the channel half-width, where the points are FreeMHD simulation results and the lines are analytical solutions using the reformulation for high Hartmann numbers.¹⁸

Likewise, the validation results for the Hunt case (conductance ratio, $c = 0.05$) are shown in Figs. 3(c) and 3(d) for the Hartmann layer and side layer, again plotting the normalized velocity profile across the channel half-width.

The flow rates for the Shercliff and Hunt cases are compared with solutions in Tables V and VI. The set velocity is used for the FreeMHD simulation flow rates, and the resulting pressure gradients along the streamwise direction are calculated. These pressure gradients are then used in the analytical solutions to find the corresponding flow rate ($Ha = 0$ case³³ and $Ha > 0$ Shercliff cases¹⁸). Finally, these solution flow rates are compared to the input simulation flow rates to find the percent error for each case. The simulation flow rate is kept constant while the magnetic field and corresponding Hartmann number are increased, which leads to increasing pressure gradients. The percent error remains low, on the order of 1% for all cases.

B. Validation with experiment: Fringing field closed pipe (closed channel, with magnetic fields)

Next, FreeMHD is compared to the experimental results of pipe flow through a fringing magnetic field for validation.³⁰ The fringing magnetic field leads to 3D pressure and current density distributions that are distinct from the fully developed solutions. The electric potential (ϕ) was measured at the walls of the pipe, and has been scaled by $\phi_0 = U_0 LB_0$. The non-dimensional electric wall potential is compared here, in Fig. 4 with $\alpha = \pm \frac{\pi}{2}$ corresponding to the left and right sides of the pipe parallel to the magnetic field. Additionally, the fully developed solution is plotted, where the experimental and simulation results at

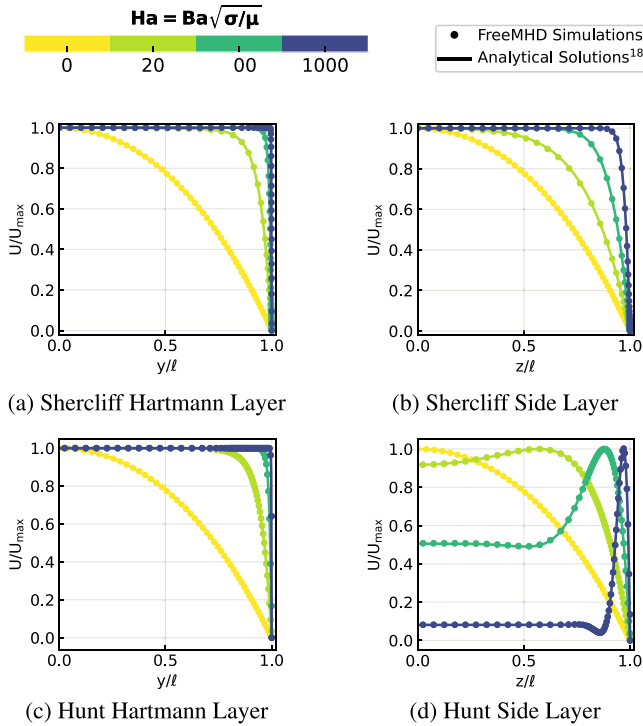


FIG. 3. Comparison to closed channel results of fully developed velocity profiles, Shercliff insulating walls ($c=0$) and Hunt conducting walls ($c=0.05$), Hartmann ($\perp B$) and side ($\parallel B$) layers. Points are FreeMHD results from the end of the channel ($x=L$), lines are analytical solutions.¹⁸ (a) Shercliff Hartmann layer, (b) Shercliff side layer, (c) Hunt Hartmann layer, and (d) Hunt side layer.

TABLE V. Shercliff case flow rates Q_{FreeMHD} (m^3/s) and pressure gradients $\text{dpdx}_{\text{FreeMHD}}$ (Pa/m) resulting from FreeMHD, with the corresponding analytical solution flow rates Q_{Solution} (m^3/s) of the $Ha=0$ case³³ and $Ha>0$ Shercliff cases¹⁸ and calculated **Percent Error** (%).

Ha	Q_{FreeMHD}	$\text{dpdx}_{\text{FreeMHD}}$	Q_{Solution}	Percent Error
0	3.89×10^{-2}	6.89×10^2	3.88×10^{-2}	0.371
20	3.89×10^{-2}	2.51×10^3	3.84×10^{-2}	1.333
100	3.89×10^{-2}	1.06×10^4	3.85×10^{-2}	1.039
1000	3.89×10^{-2}	9.94×10^4	3.86×10^{-2}	0.724

TABLE VI. Hunt case flow rates Q_{FreeMHD} (m^3/s) and pressure gradients $\text{dpdx}_{\text{FreeMHD}}$ (Pa/m) resulting from FreeMHD, with the corresponding analytical solution flow rates Q_{Solution} (m^3/s) of the $Ha=0$ case³³ and $Ha>0$ Shercliff cases¹⁸ and calculated **Percent Error** (%).

Ha	Q_{FreeMHD}	$\text{dpdx}_{\text{FreeMHD}}$	Q_{Solution}	Percent Error
0	4.70×10^{-3}	8.33×10^1	4.68×10^{-3}	0.371
20	4.70×10^{-3}	5.14×10^2	4.67×10^{-3}	0.622
100	4.70×10^{-3}	6.15×10^3	4.67×10^{-3}	0.702
1000	4.70×10^{-3}	3.91×10^5	4.63×10^{-3}	1.618

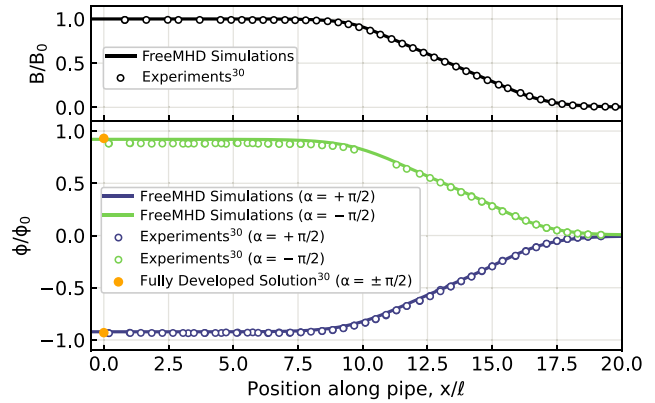


FIG. 4. Magnetic field distribution entering pipe and non-dimensional electric potential at the wall at both sides along the pipe, where $x/l=0.0$ is the magnet center, the flow enters at $x/l=20.0$, and l is the pipe radius.³⁰

$x/l=0$ in the center of the magnet demonstrate relative agreement (0.90% difference) with the fully developed solution in this region. This indicates that the fluid is becoming close to fully developed after entering the magnetic field and continuing through the uniform magnetic region toward $x/l=0$. The comparison of the non-dimensional electric wall potential shows that FreeMHD is able to accurately simulate 3D current distributions in spatially varying magnetic fields.

C. Validation with experiment: Dam breaking (free surface, no magnetic fields)

The validation of the free surface was done through comparison with a dam breaking experiment,³¹ where the evolution of the free surface can be used to validate the application of the VoF method. Here, a rectangular channel of 9 m length, 0.3 m width, and 0.34 m height was used with an initial reservoir height of $h_0 = 0.25$ m. The free surface profiles were measured optically at 50 frames/s. FreeMHD was used to calculate using a 3D domain, and the results were normalized by h_0 and plotted in Fig. 5. There is very good agreement between the experimental results and FreeMHD simulations.

D. Validation with experiment: LMX-U (free surface, with magnetic fields)

Next, MHD and free surface flows are combined for a validation case on LMX-U, a flow loop of galinstan in an open channel across an

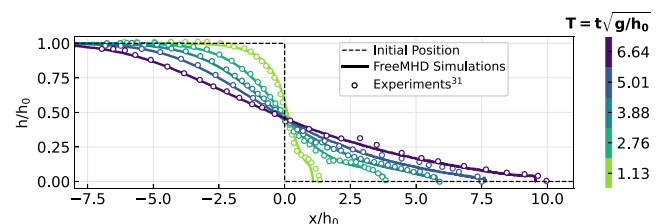


FIG. 5. Evolution of the free surface of a dam breaking,³¹ where the height and position are scaled by $h_0 = 0.25$ m.

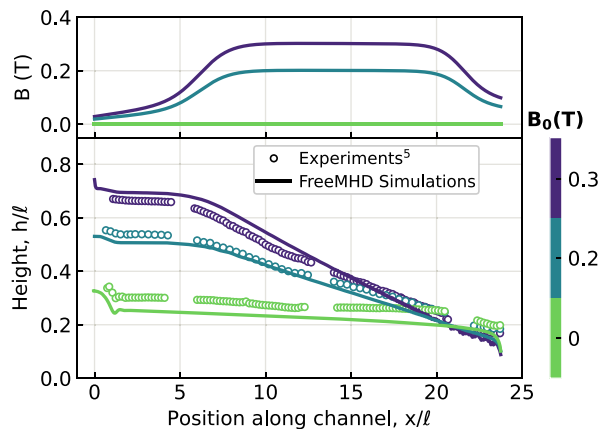


FIG. 6. LMX-U experimental measurements⁵ and FreeMHD simulation results, comparison of liquid metal profiles along the length of the channel where the flow enters at $x/l = 0$, with depths and channel locations normalized by the channel half-width (l). Additionally plotted are the magnetic field distributions used in FreeMHD simulations.

electromagnet at PPPL.⁵ The magnetic field profile is shown at the top of Fig. 6, where the flow moves across the magnet from left to right, encountering magnetic field strengths of 0, 0.2, and 0.3 T. Experiments measured the height of liquid metal using a laser-camera system, where the volumetric flow rate was kept constant. The height profile of the free surface is shown, and the simulations are plotted at the centerline along the flow direction. The FreeMHD simulation results align with experimental observations, showing the increase in the liquid metal height with the strength of the applied magnetic field. This pileup behavior is due to MHD drag, where the interaction of induced electric currents and the magnetic field generates electromagnetic forces opposing the flow. The increase in height specifically near the inlet ($x/l \leq 5$) corresponds to a reduced average velocity with increasing magnetic field strength. For example, when comparing conditions at 0 and 0.3 T, the average velocity near the inlet drops from 0.18 to 0.08 m/s. Overall, this validation with free surface MHD flow experiments demonstrates the applicability and usefulness of FreeMHD simulations.

E. Validation with experiment: Divertorlets (free surface, with magnetic fields)

The next validation case is from the paper on the experimental test device Divertorlets.³² This setup has been recreated using the FreeMHD simulations to further demonstrate the solver's main purpose in accurately modeling free-surface MHD flows. The method for velocity measurements was using a pitot tube approach, where the difference in height in tubes was correlated with the velocity of the interior flow. These main experimental measurements of the velocity between the vertical slats were compared to simulations, with the results shown in Fig. 7. Here, the average velocity between the slats is calculated and compared to the experimental results. The method of integrating across the volume center of the channel was used due to its similarity to the measurement technique. The initial conditions involve no flows and an initial volume fraction for the liquid domain around, above, and below the slats. A boundary condition for the electrodes is

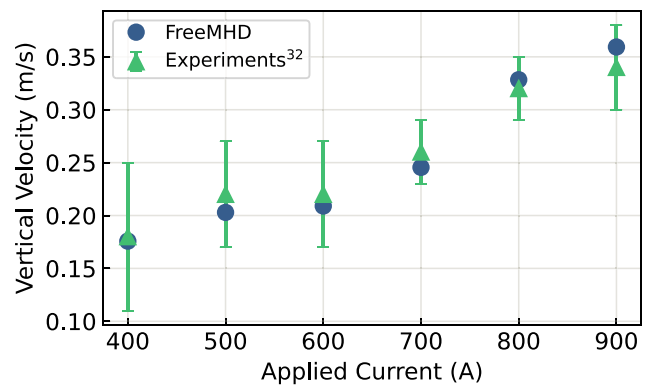


FIG. 7. Divertorlets average velocity between slats as a function of applied current for 0.2 T experiments.³²

applied using an electric potential gradient on both electrodes, as described in Sec. II B. No inlet or outlet is present in this case. The electrodes and conductors are made from copper, and there is an insulator as the floor and walls as well as between the conductor slats. As with the LMX-U case, the liquid metal used is galinstan. For a magnetic field strength of 0.2 T, the externally applied current was varied from 400 to 900 A, with both experimental and simulated results showing an increase in velocity with increased applied current.

V. DISCUSSION

An extensive number of cases have been used to verify and validate FreeMHD. By beginning with verification cases for closed flow in ducts through compared to analytical solutions, the model can be considered to be properly and accurately implemented. Next, the validation used a variety of experiments to determine the accuracy of the model compared to real-world results. The first case involved a pipe with 3D magnetic profiles, testing the ability of FreeMHD to calculate the current distribution that developed based on these conditions. Next, the dam breaking case tested the evolution of the free surface in a flow with a balance between surface tension and gravity. Finally, the LMX-U and Divertorlets cases were used to test free surface flows with magnetic fields.

A. Convergence studies

A test of mesh convergence was conducted for each of the validation cases, refining the mesh and comparing the results. This consisted of refinement of the core and boundary regions, with the resolution of the core mesh cells being the metric used for overall comparison. The validation is evaluated quantitatively using the root mean square error (RMSE) between the experimental and simulation results.

For the fringing field closed pipe case, the core was mesh refined with cases of 8, 4, 2, and 1 mm. The RMSE of the dimensionless electric potential between the positive side ($\alpha = \pm \frac{\pi}{2}$) stayed consistent with refinement between 0.0137 and 0.0139.

Next, the Dam Break case, the core region mesh was refined at cell sizes of 5, 2.5, 2, and 1.5 mm. The RMSE was calculated for the dimensionless height measurements, for each of the 5 times, and then averaged for each mesh refinement. With refinement, the RMSE

remained quite consistent, decreasing from 0.0229 to 0.0220 over the four cases from 5 to 1.5 mm.

In the LMX-U case, the core mesh was refined for cells of 4, 3, 2, and 1 mm. The RMSE was calculated for the 0.3 T case, using the dimensionless heights, resulting in a decrease from 0.045 to 0.033 over the refinement.

Finally, for the Divertorlets case, the core mesh was refined from 1.2 mm down to 0.2 mm. For this case, as single points were measured instead of profiles, a percent difference from the 400 A case velocity of 0.18 was calculated. The percent difference reduced significantly once reaching 0.4 mm to 0.91%, indicating that this resolution or below is required to accurately simulate this case.

The RMSE compared to the experiments either decreased or stayed the same upon refinement of the validation cases, indicating that the chosen resolutions were sufficient for these simulations.

B. Differences from experimental results

For the LMX-U case, in the experiment, oxides form over time on the surface of the liner and reduce the electrical conductivity, which reduces the MHD drag and LM pileup. This could explain the deviations between simulated and measured heights.

For the divertorlets case, differences from experiments can arise depending on the method for calculating the average velocity. By integrating over the volume in the center of the channels, close agreement with measurements were found. Additionally, the formation of oxides

on the liquid–gas interface can affect the surface behavior by changing the surface tension, which is not included in the model.

C. Applications

The capabilities can be demonstrated with examples of velocity and current density profiles, as seen in Fig. 8. With the flow from left to right in the streamwise profile in Fig. 8(a), this shows the velocity over the height profiles previously shown in Fig. 6. This shows how the pileup occurs near the inlet due to MHD drag, and leads the flow to become thin and accelerated toward the outlet. The cross section across the width of the duct at the midway of the magnet ($x = 0.37$ m) in Fig. 8(b), further shows how the flow overall is opposed by the Lorentz force, but the flow along the top surface is accelerated. Finally, at the same position, Fig. 8(c) shows the current density induced by the flow across the magnetic field. Here the induced current density is primarily downwards, which then recirculates through the conductive liner.

Further applications involve extending current cases to more extreme conditions, such as higher flow speeds and magnetic field strengths and the application of external current for manipulation of flows.

VI. CONCLUSIONS

FreeMHD has been validated through a series of cases, and these results confirm that FreeMHD is a reliable tool for designing LM systems under free surface conditions at the fusion reactor scale. Moreover, it is flexible, computationally efficient, and capable of solving fully 3D transient MHD flows.

Future developments for FreeMHD involve upgrades to further improve its versatility and applicability. While the currently used electric potential formulation is sufficient for the majority of liquid metal applications, some extreme conditions can necessitate magnetic field induction. Therefore, efforts are ongoing to implement a solver within FreeMHD involving an induction formulation, where the induced magnetic fields due to the currents in the fluid are included. Additionally, the solver contains the equations and ability to calculate heat transfer effects, but this will be further validated in a following paper. Finally, thermoelectric currents due to temperature gradients can be significant in a fusion environment, and will be implemented to enable further studies of these effects.

ACKNOWLEDGMENTS

This research was supported by US DOE (Grant No. DE-SC0024626).

AUTHOR DECLARATIONS

The authors have no conflicts to disclose.

Conflict of Interest

The authors have no conflicts to disclose.

Author Contributions

Brian Wynne: Investigation (equal); Validation (equal); Visualization (equal); Writing – original draft (equal); Writing – review & editing (equal). **Francisco Saenz:** Investigation (supporting); Validation

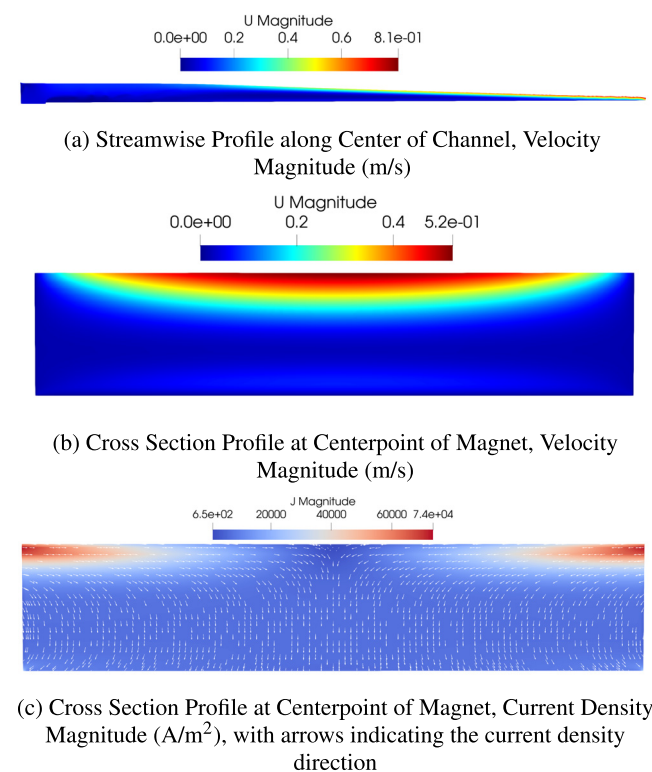


FIG. 8. Profiles of LMX-U results at 0.3 T.

(supporting); Visualization (supporting); Writing – review & editing (supporting). **Jabir Al-Salami:** Investigation (supporting); Validation (supporting); Visualization (supporting); Writing – review & editing (supporting). **Yufan Xu:** Investigation (supporting); Writing – review & editing (supporting). **Zhen Sun:** Data curation (supporting); Writing – review & editing (supporting). **Changhong Hu:** Conceptualization (supporting); Funding acquisition (supporting); Resources (supporting); Supervision (supporting). **Kazuaki Hanada:** Conceptualization (supporting); Funding acquisition (supporting); Resources (supporting); Supervision (supporting). **Egemen Kolemen:** Conceptualization (equal); Funding acquisition (equal); Supervision (equal).

DATA AVAILABILITY

The data that support the findings of this study are available in this Zenodo repository,³⁴ along with the FreeMHD GitHub repository.¹⁴

APPENDIX A: FREEMHD ALGORITHM

The FreeMHD algorithm is shown in Fig. 9.

APPENDIX B: ANALYTICAL SOLUTIONS

The reformulated analytical solutions used for the Shercliff and Hunt cases are presented in Eqs. (B1)–(B7) for the velocity distribution of a fully developed MHD flow in a rectangular duct.¹⁸ Here, a and b are the half-width of the insulating side walls and Hartmann

walls of conductivity σ_w . The aspect ratio is $l = b/a$, with conductivity ratio $d_b = (t_w \sigma_w)/(a\sigma)$, where t_w is the wall thickness and σ is the fluid electrical conductivity. The fluid velocity (V_z) is calculated using the fluid viscosity μ and pressure drop $\frac{\partial p}{\partial z}$, calculated over $\xi = x/a \in [-l, l]$ and $\eta = y/a \in [-l, l]$, where y is the direction of the magnetic field and z is the flow direction.

$$V_z = \mu^{-1} V \left(-\frac{\partial p}{\partial z} \right) a^2, \quad (\text{B1})$$

$$V = \sum_{k=0}^{\infty} \frac{2(-1)^k \cos(\alpha_k \xi)}{l \alpha_k^3} (1 - V_2 - V_3), \quad (\text{B2})$$

$$V_2 = \frac{\left(d_b r_{2k} + \frac{1 - \exp(-2r_{2k})}{1 + \exp(-2r_{2k})} \right) \frac{\exp(-r_{1k}(1-\eta)) + \exp(-r_{1k}(1+\eta))}{2}}{\frac{1 + \exp(-2r_{1k})}{2} d_b N + \frac{1 + \exp(-2(r_{1k} + r_{2k}))}{1 + \exp(-2r_{2k})}}, \quad (\text{B3})$$

$$V_3 = \frac{\left(d_b r_{1k} + \frac{1 - \exp(-2r_{1k})}{1 + \exp(-2r_{1k})} \right) \frac{\exp(-r_{2k}(1-\eta)) + \exp(-r_{2k}(1+\eta))}{2}}{\frac{1 + \exp(-2r_{2k})}{2} d_b N + \frac{1 + \exp(-2(r_{1k} + r_{2k}))}{1 + \exp(-2r_{1k})}}, \quad (\text{B4})$$

$$N = (Ha^2 + 4\alpha_k^2)^{\frac{1}{2}}, \quad (\text{B5})$$

$$r_{1k}, r_{2k} = \frac{1}{2} (\pm Ha + (Ha^2 + 4\alpha_k^2)), \quad (\text{B6})$$

$$\alpha_k = \left(k + \frac{1}{2} \right) \frac{\pi}{l}. \quad (\text{B7})$$

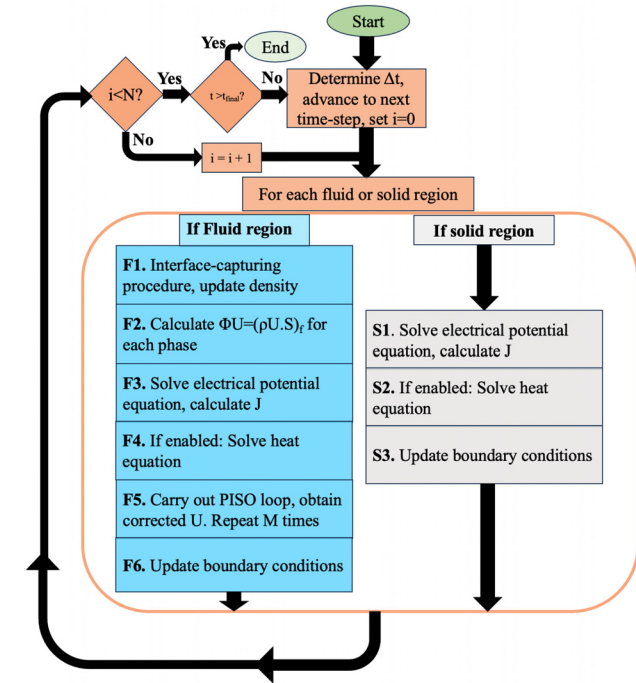


FIG. 9. FreeMHD algorithm.

REFERENCES

- ¹R. A. Pitts, X. Bonnin, F. Escourbiac, H. Frerichs, J. Gunn, T. Hirai, A. Kukushkin, E. Kaveeva, M. Miller, D. Moulton *et al.*, “Physics basis for the first ITER tungsten divertor,” *Nucl. Mater. Energy* **20**, 100696 (2019).
- ²R. Kaita, “Fusion applications for lithium: Wall conditioning in magnetic confinement devices,” *Plasma Phys. Control. Fusion* **61**, 113001 (2019).
- ³S. Krasheninnikov, L. Zakharov, and G. Pereverzev, “On lithium walls and the performance of magnetic fusion devices,” *Phys. Plasmas* **10**, 1678–1682 (2003).
- ⁴D. Boyle, R. Majeski, J. Schmitt, C. Hansen, R. Kaita, S. Kubota, M. Lucia, and T. Rognlien, “Observation of flat electron temperature profiles in the lithium tokamak experiment,” *Phys. Rev. Lett.* **119**, 015001 (2017).
- ⁵Z. Sun, J. Al Salami, A. Khodak, F. Saenz, B. Wynne, R. Maingi, K. Hanada, C. Hu, and E. Kolemen, “Magnetohydrodynamics in free surface liquid metal flow relevant to plasma-facing components,” *Nucl. Fusion* **63**, 076022 (2023).
- ⁶R. Nygren, T. Rognlien, M. Rensink, S. Smolentsev, M. Youssef, M. Sawan, B. Merrill, C. Eberle, P. Fogarty, B. Nelson *et al.*, “A fusion reactor design with a liquid first wall and divertor,” *Fusion Eng. Des.* **72**, 181–221 (2004).
- ⁷D. Gao, N. Morley, and V. Dhir, “Numerical study of liquid metal film flows in a varying spanwise magnetic field,” *Fusion Eng. Des.* **63–64**, 369–374 (2002).
- ⁸H. Huang, A. Ying, and M. Abdou, “3D MHD free surface fluid flow simulation based on magnetic-field induction equations,” *Fusion Eng. Des.* **63–64**, 361–368 (2002).
- ⁹N. Morley, S. Smolentsev, R. Munipalli, M.-J. Ni, D. Gao, and M. Abdou, “Progress on the modeling of liquid metal, free surface, MHD flows for fusion liquid walls,” *Fusion Eng. Des.* **72**, 3–34 (2004).
- ¹⁰S. Smolentsev, C. E. Kessel, J. D. Lore, R. Maingi, R. Singh, and D. L. Youchison, “Numerical analysis of liquid metal MHD flow and heat transfer for open-surface Li divertor in FNSF,” *IEEE Trans. Plasma Sci.* **50**, 4193–4198 (2022).

- ¹¹A. Khodak and R. Maingi, "Modeling of liquid lithium flow in porous plasma facing material," *Nucl. Mater. Energy* **26**, 100935 (2021).
- ¹²S. Siriano, L. Melchiorri, S. Pignatiello, and A. Tassone, "A multi-region and a multiphase MHD OpenFOAM solver for fusion reactor analysis," *Fusion Eng. Des.* **200**, 114216 (2024).
- ¹³J. S. S. A. Salami, *Numerical Simulation of MHD Free Surface Liquid Metal Flows for Nuclear Fusion Applications* (Kyuhsu University, 2022).
- ¹⁴See <https://github.com/PlasmaControl/FreeMHD> for more information about FreeMHD GitHub.
- ¹⁵J. U. Brackbill, D. B. Kothe, and C. Zemach, "A continuum method for modeling surface tension," *J. Comput. Phys.* **100**, 335–354 (1992).
- ¹⁶R. Moreau, *Magnetohydrodynamics* (Kluwer Academic Publisher, 1990), Vol. 3.
- ¹⁷U. Müller and L. Bühler, *Magnetofluidynamics in Channels and Containers* (Springer Science & Business Media, 2001).
- ¹⁸M.-J. Ni, R. Munipalli, P. Huang, N. B. Morley, and M. A. Abdou, "A current density conservative scheme for incompressible MHD flows at a low magnetic Reynolds number. Part II: On an arbitrary collocated mesh," *J. Comput. Phys.* **227**, 205–228 (2007).
- ¹⁹R. I. Issa, "Solution of the implicitly discretised fluid flow equations by operator-splitting," *J. Comput. Phys.* **62**, 40–65 (1986).
- ²⁰S. Patankar and D. Spalding, "A calculation procedure for heat, mass and momentum transfer in three-dimensional parabolic flows," *Int. J. Heat Mass Transf.* **15**, 1787–1806 (1972).
- ²¹L. Caretto, A. Gosman, S. Patankar, and D. Spalding, "Two calculation procedures for steady, three-dimensional flows with recirculation," in *Proceedings of the Third International Conference on Numerical Methods in Fluid Mechanics: Vol. II Problems of Fluid Mechanics* (Springer, 1973), pp. 60–68.
- ²²P. Moresco and T. Alboussiere, "Experimental study of the instability of the Hartmann layer," *J. Fluid Mech.* **504**, 167–181 (2004).
- ²³A. Farhadi, A. Mayrhofer, M. Tritthart, M. Glas, and H. Habersack, "Accuracy and comparison of standard $k-\epsilon$ with two variants of $k-\omega$ turbulence models in fluvial applications," *Eng. Appl. Comput. Fluid Mech.* **12**, 216–235 (2018).
- ²⁴R. Shaheed, A. Mohammadian, and H. Kheirkhah Gildeh, "A comparison of standard $k-\epsilon$ and realizable $k-\epsilon$ turbulence models in curved and confluent channels," *Environ. Fluid Mech.* **19**, 543–568 (2019).
- ²⁵N. B. Morley and J. Burris, "The MTOR LM-MHD flow facility, and preliminary experimental investigation of thin layer, liquid metal flow in a $1/r$ toroidal magnetic field," *Fusion Sci. Technol.* **44**, 74–78 (2003).
- ²⁶W. J. O'Donnell, P. G. Papanikolaou, and C. B. Reed, "The thermophysical and transport properties of eutectic NAK near room temperature," Technical Report No. ANL/FPP/TM-237, 1989.
- ²⁷H. W. Davison, *Compilation of Thermophysical Properties of Liquid Lithium* (National Aeronautics and Space Administration, 1968), Vol. 4650.
- ²⁸J. Shercliff, "Steady motion of conducting fluids in pipes under transverse magnetic fields," in *Mathematical Proceedings of the Cambridge Philosophical Society* (Cambridge University Press, 1953), Vol. 49, pp. 136–144.
- ²⁹J. Hunt, "Magnetohydrodynamic flow in rectangular ducts," *J. Fluid Mech.* **21**, 577–590 (1965).
- ³⁰L. Bühler, H.-J. Brinkmann, and C. Mistrangelo, "Experimental investigation of liquid metal pipe flow in a strong non-uniform magnetic field," *Magnetohydrodynamics* **56**, 0024–998X (2020).
- ³¹H. Ozmen-Cagatay and S. Kocaman, "Dam-break flows during initial stage using SWE and RANS approaches," *J. Hydraulic Res.* **48**, 603–611 (2010).
- ³²F. Saenz, Z. Sun, A. E. Fisher, B. Wynne, and E. Kolemen, "Divertorlets concept for low-recycling fusion reactor divertor: Experimental, analytical and numerical verification," *Nucl. Fusion* **62**, 086008 (2022).
- ³³R. K. Shah, A. London, and F. M. White, "Laminar flow forced convection in ducts," *J. Fluids Eng.* **102**(2), 256–257 (1980).
- ³⁴B. Wynne and E. Kolemen, "Input files and processed results for FreeMHD: Validation and verification of the open-source, multi-domain, multi-phase solver for electrically conductive flows," Zenodo Repository, 2024.